processes

MDPI

Article

High-Density Polyethylene Pipe Butt-Fusion Joint Detection via Total Focusing Method and Spatiotemporal Singular Value Decomposition

Haowen Zhang [1], Qiang Wang [1,*], Juan Zhou [1], Linlin Wu [1], Weirong Xu [2] and Hong Wang [2]

[1] College of Energy Environment and Safety Engineering, China Jiliang University, Hangzhou 310018, China; p22060857044@cjlu.edu.cn (H.Z.); zhoujuan@cjlu.edu.cn (J.Z.); wulinlin@cjlu.edu.cn (L.W.)
[2] Huzhou Special Equipment Inspection and Research Institute, Huzhou 313099, China; wh@hztjzx.cn (W.X.); 19957222673@sohu.com (H.W.)
* Correspondence: qiangwang@cjlu.edu.cn

Abstract: High-density polyethylene (HDPE) pipes are widely used for urban natural gas transportation. Pipes are usually welded using the technique of thermal butt fusion, which is prone to manufacturing defects that are detrimental to safe operation. This paper proposes a spatiotemporal singular value decomposition preprocessing improved total focusing method (STSVD-ITFM) imaging algorithm combined with ultrasonic phased array technology for non-destructive testing. That is, the ultrasonic real-value signal data are first processed using STSVD filtering, enhancing the spatiotemporal singular values corresponding to the defective signal components. The TFM algorithm is then improved by establishing a composite modification factor based on the directivity function and the corrected energy attenuation factor by adding angle variable. Finally, the filtered signal data are utilized for imaging. Experiments are conducted by examining specimen blocks of HDPE materials with through-hole defects. The results show the following: the STSVD-ITFM algorithm proposed in this paper can better suppress static clutter in the near-field region, and the average signal-to-noise ratios are all higher than the TFM algorithm. Moreover, the STSVD-ITFM algorithm has the smallest average error among all defect depth quantification results.

Keywords: high-density polyethylene pipe joints; ultrasonic phased array; total focusing method; spatiotemporal singular value decomposition; filter processing

Citation: Zhang, H.; Wang, Q.; Zhou, J.; Wu, L.; Xu, W.; Wang, H. High-Density Polyethylene Pipe Butt-Fusion Joint Detection via Total Focusing Method and Spatiotemporal Singular Value Decomposition. *Processes* **2024**, *12*, 1267. https://doi.org/10.3390/pr12061267

Academic Editors: Diane Mynors and Qingping Yang

Received: 22 May 2024
Revised: 14 June 2024
Accepted: 17 June 2024
Published: 19 June 2024

1. Introduction

High-density polyethylene (HDPE) pipes, due to good chemical properties and mechanical strength, such as corrosion resistance, toughness, long service life, etc., have been widely used in urban natural gas supply system [1–3]. In the process of urban gas transportation, several HDPE pipes need to be connected, and joint welding using the thermal butt-fusion technique is a common means of pipes connection [4,5]. Butt-fusion joints are the weakest link of the HDPE pipes, which determine the safety performance of the whole pipeline system. During the butt-fusion welding process of HDPE pipe joints, improper adjustment of welding parameters (e.g., temperature, pressure, and duration of heating, etc.) and contamination of the material surface are prone to result in a number of manufacturing defects [6–8]. These manufacturing defects include through-holes, inclusions, and lack of fusion. In addition, poor workmanship during on-site installation, repair, and maintenance of piping may also lead to defects [9,10]. These defects of butt-fusion joints will increase the risk of structural failure or critical damage to the HDPE pipes, which is detrimental to the sustainability of the whole pipeline systems. It may even lead to gas leakage, resulting in safety accidents and economic losses. In order to safeguard the weld

quality of HDPE pipe butt-fusion joints from structural failure, non-destructive evaluation (NDE) using a number of intelligent inspection tools is essential [11,12].

Ultrasonic phased array inspection technology is a widely used method in NDE, known for its effectiveness in identifying defects and quantitatively characterizing HDPE materials [7,13–17]. The total focusing method (TFM), based on the full matrix capture (FMC) technique, has now become a golden rule for post-processing of ultrasonic phased array inspection. The TFM algorithm utilizes a delay and sum (DAS) beam synthesis method to focus the ultrasonic signal into a predefined grid region for imaging [18]. However, the viscoelastic properties of HDPE materials cause scattering and absorption of ultrasonic waves during propagation, resulting in reduced signal amplitude, lower signal-to-noise ratio (SNR), and decreased quality in TFM images [19].

Singular value decomposition (SVD) has now been shown to be useful in the field of NDE for signal extraction as well as image optimization [20–22]. After SVD processing, the defect signal is often distinguished from noise. This is due to the fact that the defect signal has a large energy share and corresponds to larger singular values, whereas noise corresponds to smaller singular values [23,24]. Zhang et al. [25], in the detection of circular hole defects in noisy metallic materials, utilized high-order SVD to directly process FMC data. Then, the processed signal data are imaged with the ultrasonic reverse time migration imaging method, and the method can effectively suppress the structural noise. Rao et al. [26], in the detection of defects in side-drilled holes of HDPE piping materials, proposed an improved TFM algorithm utilizing FIR filters as well as block-wise SVD processing, which can effectively suppress near-field clutter and background noise. In the field of medical ultrasonic imaging, an advanced spatiotemporal singular value decomposition (STSVD) filtering method is used to optimize images [27]. The 3D medical ultrasonic complex-valued signal data are first converted into a 2D Casorati matrix, including the spatial dimension (compounding the depth z-direction of the ultrasonic transducer and the x-direction of the number of samples) and the temporal dimension (temporal sampling), and are then subjected to SVD processing. Based on the difference in spatiotemporal coherence of the signal components, it is important to set both higher-order and lower-order cutoffs. By selecting the most favorable spatiotemporal singular values for reconstruction, it becomes possible to effectively suppress noise and artifacts [28,29]. Rao et al. [30]applied the STSVD method to TFM imaging of HDPE piping materials. They initially demodulated the FMC real-valued signal data, converted them to complex-valued data similar to medical ultrasonic signals. Subsequently, they utilized STSVD filtering and implemented imaging with the TFM algorithm. This method is more conducive to noise suppression. However, there are still relatively few studies related to the optimization of TFM images of HDPE piping materials using STSVD. In addition, the directivity function of the array element in the sound field characterizes the mapping between the energy intensity of the ultrasonic waves and the direction of propagation [31] . The TFM image is optimized by establishing a compensation factor based on the directivity function, taking into account the energy attenuation of ultrasonic waves. It has a better effect of suppressing the structural noise and improving the SNR in ultrasonic phased array inspection of high-attenuation metal coarse-crystalline materials [32,33] . However, there are also fewer studies on the application of this method to ultrasonic phased array inspection of HDPE piping materials.

The contribution is that, to ensure the weld quality of HDPE pipe butt-fusion joints, this paper proposes a spatiotemporal singular value decomposition preprocessing improved total focusing method (STSVD-ITFM) imaging algorithm combined with ultrasonic phased array technology. The algorithm consists of three important steps, the first step is setting the enhancement factor to enhance the spatiotemporal singular values corresponding to the defective signal components when filtering the FMC real-valued signal data directly using STSVD. The second step is improving the TFM pixel point amplitude based on the composite modification factor, which is composed of the directivity factor and the energy attenuation factor corrected by adding the angle variable. Finally, the

STSVD-filtered FMC data matrix is then processed for the improved TFM imaging. To evaluate the effectiveness of the algorithm proposed in this study, experiments are carried out on a test block made of HDPE material. The imaging results are then compared with the TFM algorithm, the STSVD processing TFM algorithm (STSVD-TFM), and the improved TFM (ITFM) algorithm introduced in this paper.

The remainder of this paper is structured as follows: The second section describes the theory of the algorithms, including the overall architecture of FMC data, the principle of STSVD filtering, the principle of the ITFM algorithm, the STSVD-TFM algorithm, and the implementation of the ITFM algorithm. The third section includes the experiments, including the HDPE test block and experimental equipment. It also mentions the extraction of ultrasonic signals from specific transmit–receive array element combinations in the FMC data, filtering them with STSVD. The fourth section includes the imaging results, comparing and analyzing images generated using the four algorithms with relevant imaging data. The final section includes the conclusions.

2. Principles of Algorithms

2.1. The Ultrasound Phased Array Data Based on FMC

The FMC technique is a more advanced way of acquiring signal data based on ultrasonic phased array probes. In a one-dimensional linear ultrasonic array with N array elements, the FMC technique sequentially excites each array element and receives the ultrasonic signal from all of them. This process follows a one-transmit–one-receive mode until the Nth array element both excites and receives the ultrasonic signal [34]. The process is shown in Figure 1.

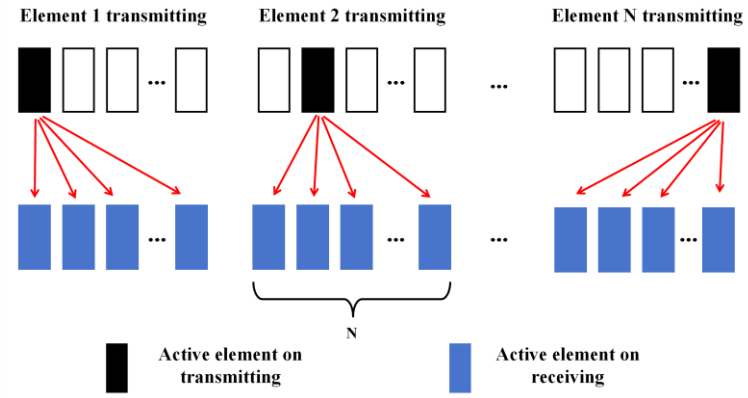

Figure 1. Process of acquiring ultrasonic signal data using FMC technology.

The acquired ultrasonic signal is represented by a 3D real-valued matrix of dimension (N, N, N_S), denoted as $u(x_t, x_r, t_{Ns})$. Where x_t and x_r are the positions of the transmitter and receiver of the array element, respectively. t is the propagation time, and N_S is the number of sampling points. Then, the corresponding time series signal data at a given moment can be expressed as follows:

$$u(x_t, x_r, t) = \begin{bmatrix} u(x_1, x_1, t) & u(x_1, x_2, t) & \cdots & u(x_1, x_N, t) \\ u(x_2, x_1, t) & u(x_2, x_2, t) & \cdots & u(x_2, x_N, t) \\ \vdots & \vdots & \ddots & \vdots \\ u(x_N, x_1, t) & u(x_N, x_2, t) & \cdots & u(x_N, x_N, t) \end{bmatrix} \quad (1)$$

The 3D distribution of the FMC data is shown in Figure 2.

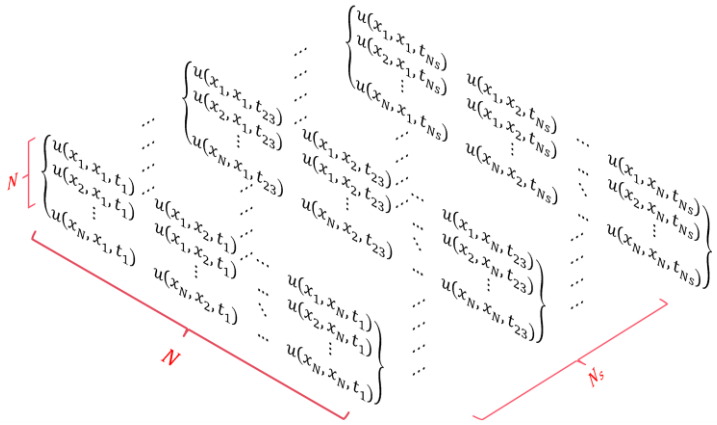

Figure 2. 3D distribution of FMC data.

2.2. STSVD Filtering Processing

The biggest difference between the STSVD and the conventional SVD processing is that the STSVD focuses on the 2D Casorati matrix consisting of spatial and temporal samples. The data acquired using the FMC technique can be considered as a coupling of the ultrasonic signal in the spatial and temporal dimensions, so the FMC data matrix is transformed into a two-dimensional Casorati matrix of dimension S [27,29]. Processing of matrix S using STSVD:

$$S = U\Delta V^{*} \tag{2}$$

where $U = [u_1, u_2, \ldots, u_i, \ldots, u_{N^2}]$ is the left singular vector of the matrix S, also known as a spatial singular vector, it has dimension (N^2, N^2) and any u_i denotes a column vector of dimension $N^2 \times 1$. Δ is an affine matrix of dimension (N^2, N_S) with diagonal elements $[\sigma_1, \sigma_2, \cdots, \sigma_i, \cdots, \sigma_r]$ and arranged in descending order, r is the rank of the matrix S, and the rest of the elements are 0. $V = [v_1, v_2, \ldots, v_i, \ldots, v_{N_S}]$ is the right singular vector of the matrix S, also known as the temporal singular vectors of dimension (N_S, N_S), and any v_i denotes a column vector of dimension $N_S \times 1$.

This is based on the key assumptions that the components of the ultrasonic signal are not uniformly sensitive to spatiotemporal coherence and that the spatiotemporal coherence of the signal can be characterized by temporal singular vectors V. Therefore, spatiotemporal filtering of signal data using STSVD makes the enhancement of defects as well as the suppression of noise possible. The static clutter in the near-field region exhibits high amplitude and low spatiotemporal coherence, which corresponds to lower-order singular values. In contrast, noise exhibits low amplitude and higher spatiotemporal coherence, corresponding to higher order singular values [28,30]. The spatiotemporal filtering of signal is realized by setting low-order and high-order cutoffs to filter out the singular values and singular vectors of a defective signal. The cutoff is chosen based on the singular value order in the singular value spectrum.

Filtering the singular values corresponding to defective signals based on the low-order and high-order cutoff:

$$\Delta^{ST} = \Delta \times I^{ST} \tag{3}$$

where I^{ST} is a diagonal matrix whose elements consist of 0 and 1, in which the elements between the low-order cutoff r_{st} and the high-order cutoff r_{gt} are 1 and the rest are 0. To enhance the strength of the signal of the defect, set the enhancement factor μ. Figure 3 shows the singular value spectrum of FMC data of an HDPE material after STSVD processing. The positions of r_{st} and r_{gt} are labeled, and the matrix Δ^{ST} that corresponding to the selected defective signal is composed of the singular values between them. The red

curve represents the singular value matrix $(\Delta^{ST})^{\mu}$ enhanced by μ. It is worth noting that, unlike the processing done in the literature [30], this paper utilizes STSVD to process the FMC real-valued data directly, which leads to a larger difference between r_{st} and r_{gt}, but does not have too much effect on the filtered results (see Sections 3.3 and 4.1 below for details).

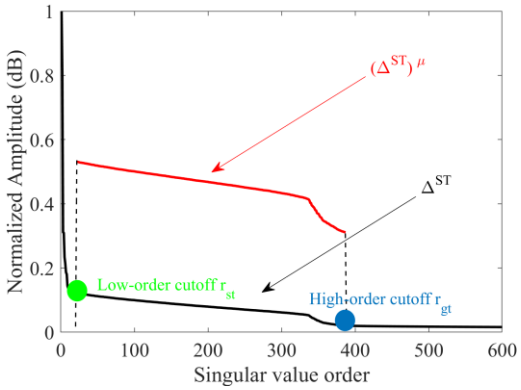

Figure 3. Singular values spectrum of FMC data of an HDPE material processed using STSVD.

Then, the inverse STSVD calculation is performed to obtain the filtered Casorati matrix S^{ST}:

$$S^{ST} = U\left(\Delta^{ST}\right)^{\mu} V^{*} \tag{4}$$

Finally, the spatiotemporally filtered 2D Casorati matrix S^{ST} is converted into a 3D FMC data matrix $u^{ST}(x_t, x_r, t_{Ns})$ with dimensions (N, N, N_S).

2.3. Improved Total Focusing Method

The TFM algorithm is derived from the beam synthesis method DAS. It involves a time-delayed superposition of the acquired FMC ultrasonic signal data, which is then synthesized and focused to produce an imaging effect in a specified grid region, as illustrated in Figure 4 [18]. The pixel amplitude $I_{TFM}(x, z)$ of any imaging point $P(x, z)$ in the grid can be expressed as follows:

$$I_{TFM}(x,z) = \left| \sum_{t=1}^{N} \sum_{r=1}^{N} H\left(u\left(x_t, x_r, t_{Ns}\right)\right) \right| \tag{5}$$

where H denotes the Hilbert transform. Then, the pixel point amplitude obtained by performing the TFM operation on the FMC data that has been processed using the STSVD filtering is as follows:

$$I_{STSVD-TFM}(x,z) = \left| \sum_{t=1}^{N} \sum_{r=1}^{N} H\left(u^{ST}\left(x_t, x_r, t_{Ns}\right)\right) \right| \tag{6}$$

When array elements excite ultrasonic waves in the sound field, there is some kind of mapping between its energy intensity and the propagation direction of the sound beam, which can be characterized by the directivity function. Then, build the directivity factor $D_{t,r}(x, z)$ based on the following function [31,33]:

$$D_{t,r}(x,z) = \operatorname{sinc}\left(\frac{d_0 \cdot \pi \cdot \sin\left(\theta_{t,p}\right)}{\lambda}\right) \cdot \operatorname{sinc}\left(\frac{d_0 \cdot \pi \cdot \sin\left(\theta_{r,p}\right)}{\lambda}\right) \tag{7}$$

where d_0 is the width of a single array element. $\theta_{t,p}$ and $\theta_{r,p}$ are the angles between the array elements t, r, and $P(x, z)$ in the OZ direction of the coordinate axis. And λ denotes the wavelength.

The attenuation of ultrasonic energy is related to the distance from the array element to the imaging point, so the energy attenuation factor can be approximated as follows [33]:

$$E_{t,r}(x,z) = \frac{1}{\sqrt{d_{t,p} \cdot d_{r,p}}} \tag{8}$$

where $d_{t,P}$ and $d_{r,P}$ are the distance between the array elements t, r, and $P(x, z)$, respectively. From the directivity function, it can be seen that the attenuation of ultrasonic energy is also related to the direction of propagation of the acoustic beam. The cosine of the angle between the array element and the imaging point serves as an angular variable for correcting $E_{t,r}(x, z)$:

$$E_{t,r}{}'(x,z) = \frac{c\left|\cos\left(\theta_{t,p}\right)\cdot\cos\left(\theta_{r,p}\right)\right|^{\frac{3}{2}}}{2\pi\lambda} \cdot E_{t,r}(x,z) \tag{9}$$

where $E_{t,r}'(x, z)$ is the corrected energy attenuation factor. c is the speed of ultrasonic waves propagating in the HDPE materials. The composite modification factor $M_{t,r}(x, z)$ is established based on $D_{t,r}(x, z)$ and $E_{t,r}'(x, z)$:

$$M_{t,r}(x,z) = \left|\frac{D_{t,r}(x,z)\cdot E_{t,r}{}'(x,z)}{2}\right| \tag{10}$$

The improved pixel point amplitude matrix $I_{ITFM}(x, z)$ is obtained by weighting $I_{TFM}(x, z)$ by $M_{t,r}(x, z)$:

$$I_{ITFM}(x,z) = \left|\sum_{t=1}^{N}\sum_{r=1}^{N} M_{t,r}(x,z)\cdot I_{TFM}(x,z)\right| \tag{11}$$

Then, the pixel point amplitude obtained by performing the ITFM operation on the FMC data that have been processed using the STSVD filtering is as follows:

$$I_{STSVD-ITFM}(x,z) = \left|\sum_{t=1}^{N}\sum_{r=1}^{N} M_{t,r}(x,z)\cdot H\left(u^{ST}\left(x_t,x_r,t_{Ns}\right)\right)\right| \tag{12}$$

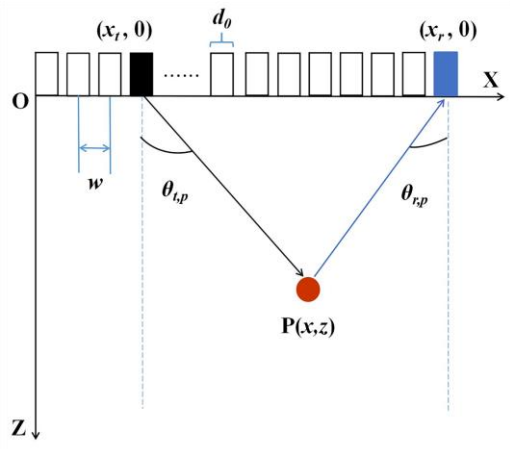

Figure 4. Schematic of the TFM imaging area.

3. Experiments

In this paper, an HDPE plate test block is selected for ultrasonic phased array defect detection experiments, which is made of PE100, and its specification is 400 mm × 40 mm × 80 mm. The physical and structural diagrams of the test block are shown in Figure 5. The HDPE test blocks contained three sizes of through-hole defects located from 10 mm to 50 mm in depth. There are 9 defects each of 1 mm and 2 mm diameter, and the depth

interval between adjacent defects is 5 mm. Defects with a diameter of 3 mm contain 5 defects, with a depth interval of 10 mm between adjacent defects.

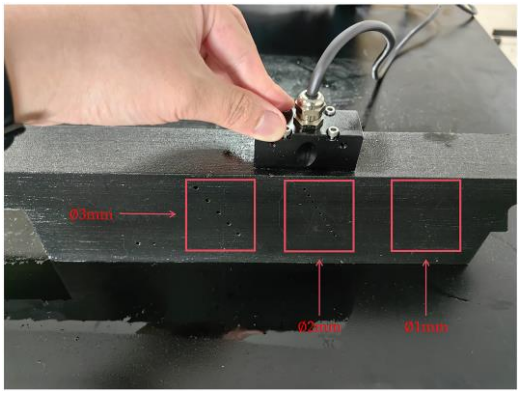

(**a**)

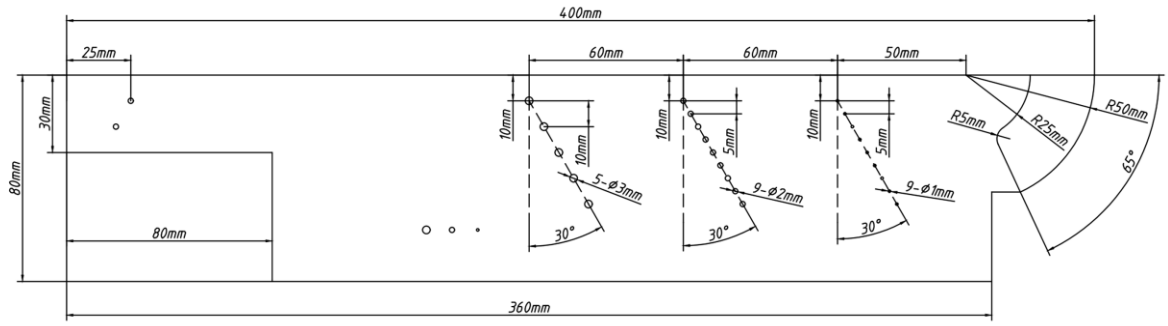

(**b**)

Figure 5. HDPE test block physical and structural diagrams: (**a**) physical diagram and (**b**) structural diagram.

In this paper, the one-dimensional linear ultrasound array is used for the detection experiments, and the placement of the phased array probe is shown in Figure 5a. Its associated acquired and processed ultrasonic parameters are shown in Table 1.

Table 1. Associated acquired and processed ultrasonic parameters for the experiment.

Associated Acquired and Processed Ultrasonic Parameters	Value
Number of active array elements in the probe	64
The active array element width	0.6 mm
The active array element pitch	0.75 mm
Center frequency	2.25 MHz
Sampling frequency	62.5 MHz
Excitation voltage	100.0 V
The signal pulse width	300.0 ns
Sound velocity	2300.0 m/s

3.1. A-Scan Signal Analysis

The FMC data contain the ultrasonic echo A-Scan signal from all combinations of transmit–receive arrays that carry complete information about the defects. Figure 6 demonstrates the ultrasonic echo signal of the (16, 48) array element combination (the 16th array element excites the signal and the 48th array element receives) for 1 mm diameter through-hole defects in the HDPE test block. Figure 6 shows the time-domain information

of this echo signal, revealing significant static clutter in the ultrasonic near-field area with a wide range of amplitude. The presence of through-hole defects can be observed based on the echo of the ultrasonic signal. Particularly, the adverse impact of interference on through-hole defects no. 1 and no.2 in the near-field region due to its proximity to the probe can be observed. This interference leads to a degradation of the echo signal from the defective area. However, in the no. 3 to no. 5 through-hole defects, which are situated far from the near-field region, the echo signal is significantly heightened, thus aiding in the identification of the defects. As the depth of defects increases, the viscoelastic attenuation of the HDPE test block also increases. This results in a decrease in the amplitude of the echo signal for no. 6 and the later through-hole defects. Specifically, the amplitude decrease is more significant for the no. 7, no. 8, and no. 9 through-hole defects. In the case of the no. 9 through-hole defect, the echo signal is completely overshadowed by surrounding noise.

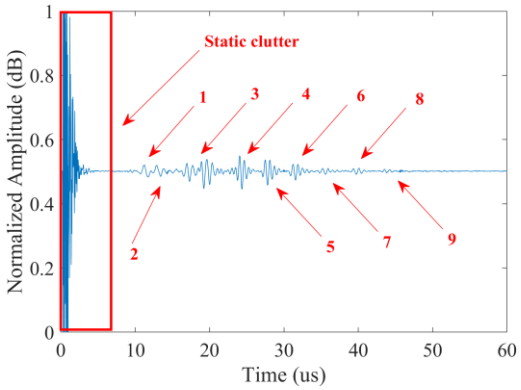

Figure 6. A-Scan signal of (16, 48) array element combination ultrasonic echo.

3.2. STSVD Signal Filtering

The key to filtering the FMC signal data using STSVD lies in the selection of the low-order cutoff r_{st} and high-order cutoff r_{gt}. r_{st} corresponds to the signal component with low spatiotemporal coherence, which controls the effective suppression of static clutter. r_{gt} corresponds to the signal component with high spatiotemporal coherence, which ensures the integrity of the defective signal. To verify the performance of r_{st} for the suppression of static clutter and r_{gt} for the ability to characterize the integrity of the defects, this paper is designed to filter the ultrasonic echo signal using a (16, 48) array element combination for 1 mm diameter through-hole defects with different values. The signal filtering is shown in Figures 7 and 8.

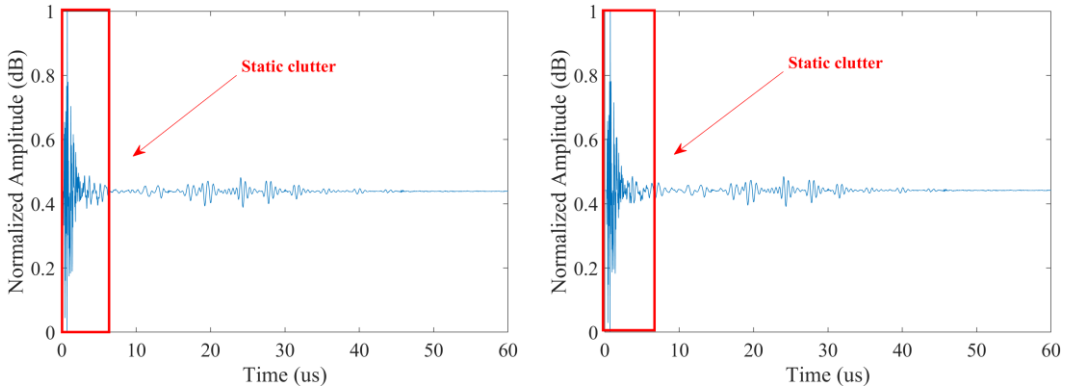

(**a**) r_{st} = 5 (**b**) r_{st} = 10

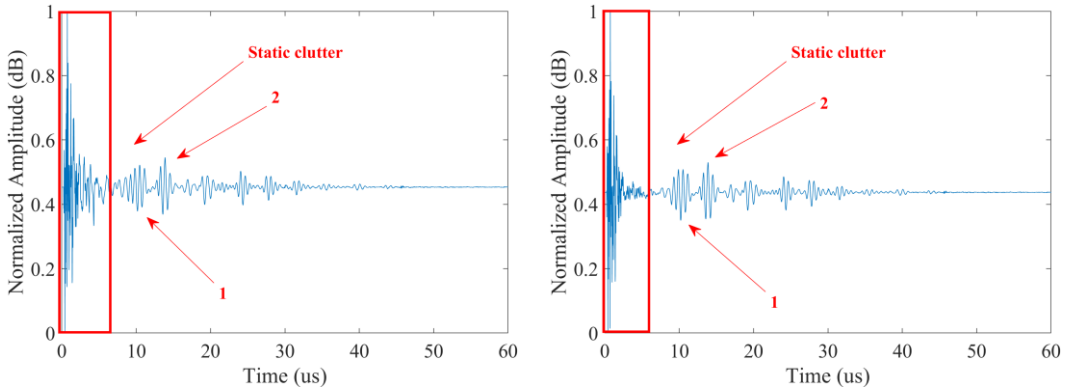

(**c**) r_{st} = 15 (**d**) r_{st} = 20

Figure 7. Filtering of (16, 48) array element combination ultrasonic echo with different r_{st} values 5, 10, 15 and 20 respectively: (**a**) r_{st} = 5; (**b**) r_{st} = 10; (**c**) r_{st} = 15; and (**d**) r_{st} = 20. The filtering is achieved by reconstructing the matrix Δ^{ST} using only the singular values after the r_{st} value

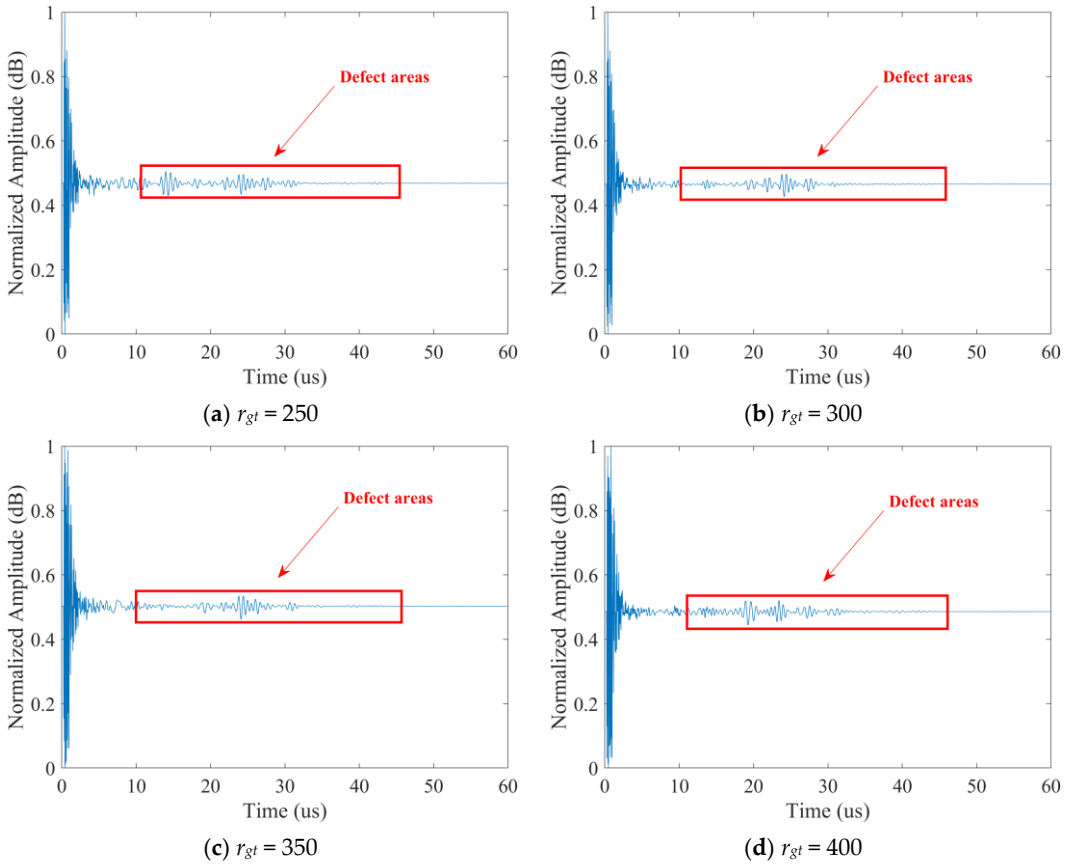

(**a**) r_{gt} = 250 (**b**) r_{gt} = 300

(**c**) r_{gt} = 350 (**d**) r_{gt} = 400

Figure 8. Filtering of (16, 48) array element combination ultrasonic echo with different r_{gt} values 250, 300, 350 and 400 respectively: (**a**) r_{gt} = 250, (**b**) r_{gt} = 300, (**c**) r_{gt} = 350, and (**d**) r_{gt} = 400. The filtering is achieved by reconstructing the matrix Δ^{ST} retaining the singular values between the first value and the r_{gt} value.

Figure 7 illustrates the signal filtering for r_{st} = 5, 10, 15, and 20, respectively. Only the singular values before the value of r_{st} are eliminated, and the remainder are used to reconstruct the matrix Δ^{ST}. By comparing with the original ultrasonic echo signal (Figure 6), the static clutter amplitude is reduced in Figure 7, and it can be seen that the low-order cutoff is beneficial to static clutter suppression. Notably, in Figure 7c,d, the amplitudes of the no. 1 and no. 2 through-hole defects are significantly improved, which improves the

recognition of the defects. Figure 8 illustrates the filtering with the values of r_{gt} set to 250, 300, 350, and 400, respectively. The reconstruction of the matrix Δ^{ST} is performed by retaining the singular values between the first value and the r_{gt} value. Low-order singular values are retained, resulting in static clutter that is not well suppressed. Changing the selection of higher-order singular values affects the integrity of the defects and their surrounding noise. The high value of r_{gt} allows a large number of singular values containing noisy information to be used for matrix Δ^{ST} reconstruction.

Setting the r_{st} value to 21 and the r_{gt} value to 387 for reconstructing the singular value matrix Δ^{ST}, the obtained STSVD filtered processed (16, 48) array element combination ultrasonic echo signal is shown in Figure 9, where the blue curve represents the echo signal after filtering using the singular value matrix Δ^{ST} intercepted by r_{st} and r_{gt}. The red curve represents the echo signal after filtering using the singular value matrix $\left(\Delta^{ST}\right)^{\mu}$ enhanced by μ. As can be seen from Figure 9, both filtering methods have better suppression of static clutter in the near-field region compared to the original echo signal (Figure 6). Each defect can be completely characterized, and both can increase the amplitude of the no. 1 and no. 2 through-hole defects. In addition, the singular value matrix $\left(\Delta^{ST}\right)^{\mu}$ enhanced by μ can improve the overall signal amplitude level without losing signal components when reconstructing the echo signal.

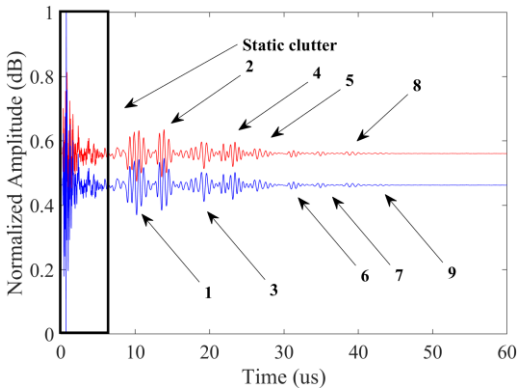

Figure 9. Processing of (16, 48) combination of array elements ultrasonic echo signal using STSVD filtering. The blue curve represents filtering using the singular value matrix Δ^{ST}, and the red curve represents filtering using the singular value matrix $\left(\Delta^{ST}\right)^{\mu}$. Furthermore, the locations of the defects are labeled in the figure.

4. Results and Discussion

4.1. Comparison of Imaging Results

The imaging results of different algorithms for the HDPE test block with 1 mm, 2 mm, and 3 mm diameter through-hole defects are shown in Figure 10, Figure 11, and Figure 12, respectively. It should be clarified that the $\left(\Delta^{ST}\right)^{\mu}$ processing is applied in all the filtering of FMC inspection data using STSVD, which utilizes μ to enhance the filtered defective signal singular value matrix. In the imaging of through-hole defects with 1 mm diameter, r_{st} is set to 21 and r_{gt} to 387. In the imaging of through-hole with 2 mm and 3 mm diameter, r_{st} is set to 10 and r_{gt} to 360. For the setting of low-order and high-order cutoff, it is only applied for the HDPE test block in this paper.

In the imaging results for a 1 mm diameter through-hole defects shown in Figure 10, the conventional TFM algorithm (Figure 10a) can present the locations of all defects. Due to the viscoelastic attenuation property of HDPE materials, the defect amplitude gradually decreases with depth, which is more obvious with the no. 6 to no. 9 through-hole defects. There is a large number of static clutter in the near-field region of higher amplitude at the

top of the image, which is consistent with the ultrasonic echo signal demonstrated in Figure 6. In addition, the no. 1 through-hole defect is relatively heavily contaminated by noise due to its proximity to static clutter. Figure 10b shows the imaging result of the TFM algorithm after the STSVD filtering process, and it can be seen that the static clutter amplitude at the top of the image is reduced. However, the no. 1 through-hole defect is still contaminated with noise and the amplitude of the no. 7 to no. 9 through-hole defects is substantially lower than that of the TFM image. Figure 10c shows the imaging result of the ITFM algorithm with lower static clutter amplitude than the TFM and STSVD-TFM images. The no. 5 to no. 9 through-hole defects amplitudes are elevated, especially for the no. 7 to no. 9 defects where the amplitude is more significantly elevated compared to the TFM and STSVD-TFM images. The ITFM algorithm considers the impact of directivity and ultrasonic energy attenuation, and in this way improves the TFM algorithm. Nevertheless, numerous artifacts emerge below a depth of approximately 35 mm, due to the boost of the amplitude of the defects at that depth, which also causes the amplitude of the background noise to rise to a high level. Figure 10d shows the imaging results of applying STSVD filtering processing to the ITFM algorithm. The STSVD-ITFM algorithm reduces the amplitude of the static clutter on the basis of the ITFM image, which is better suppressed. It also reduces the background noise at a depth of about 35 mm in the ITFM image and suppresses artifacts. Relatively, the no. 6 to no. 9 through-hole defects' amplitudes at this depth are also lower than the ITFM image. However, these defects' amplitudes are still higher than TFM and STSVD-TFM images.

Figures 11 and 12 show the imaging of 2 mm and 3 mm diameter through-hole defects, where the performance of the imaging algorithms is nearly identical to the 1 mm diameter imaging results. Conventional TFM images (Figures 11a and 12a) still have higher amplitude static clutter above them, and the defect amplitude gradually decreases with increasing depth. The STSVD-TFM algorithm reduces the amplitude level of the static clutter, but the amplitude of the no. 7 to no. 9 through-hole defects in Figure 11b and the no. 4 to no. 5 defects in Figure 12b are lower than the corresponding TFM images. The ITFM algorithm effectively reduces static clutter while increasing the amplitude level of defects at deeper locations. However, it also increases the amplitude of background noise surrounding the defects. A large number of artifacts began to appear at a depth of about 43 mm (Figures 11c and 12c). The STSVD-ITFM algorithm can enhance the advantage of suppressing static clutter based on the ITFM algorithm, while improving the disadvantage that the ITFM algorithm can introduce a lot of noise. Although the amplitude of defects at deeper locations is reduced, it is still higher than the STSVD-TFM image.

In summary, the conventional TFM algorithm is vulnerable to static clutter in the near-field region and viscoelastic attenuation. While the STSVD filtering can decrease the amplitude of static clutter, it is important to note that the amplitude of defects in deeper locations affected by viscoelastic attenuation should be lower. The ITFM algorithm shows better suppression of static clutter as well as strong carry fading ability but is less robust to background noise. The STSVD-ITFM algorithm provides the best suppression of static clutter and improves the drawback of the ITFM algorithm's poor robustness to background noise. However, the fading resistance is weaker than the ITFM algorithm, yet still higher than the STSVD-TFM algorithm.

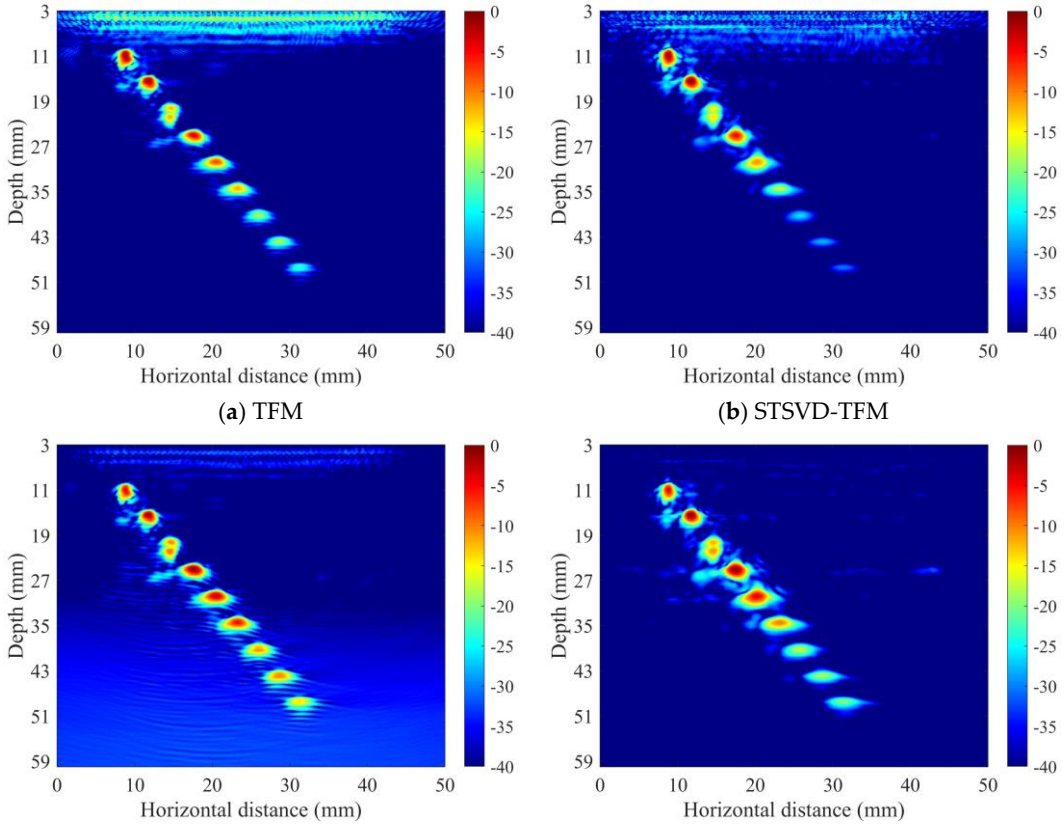

(**a**) TFM (**b**) STSVD-TFM

(**c**) ITFM (**d**) STSVD-ITFM

Figure 10. Imaging results of 1 mm diameter through-hole defects (no. 1 to no. 9).

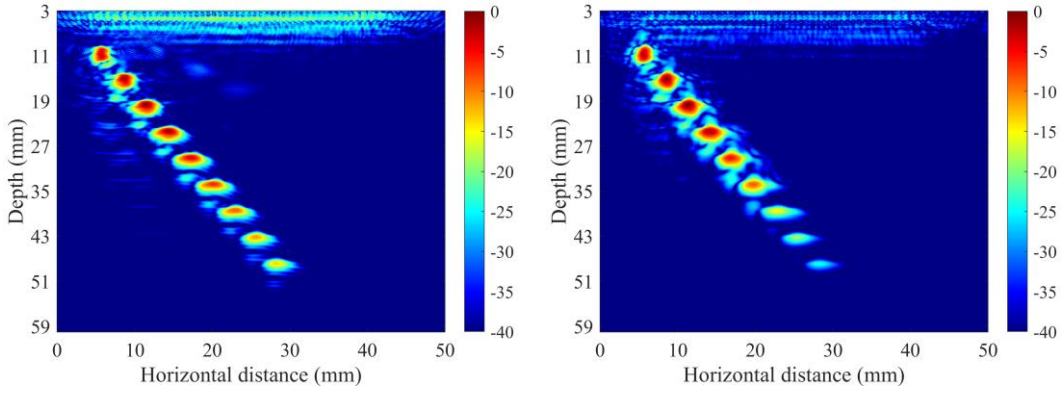

(**a**) TFM (**b**) STSVD-TFM

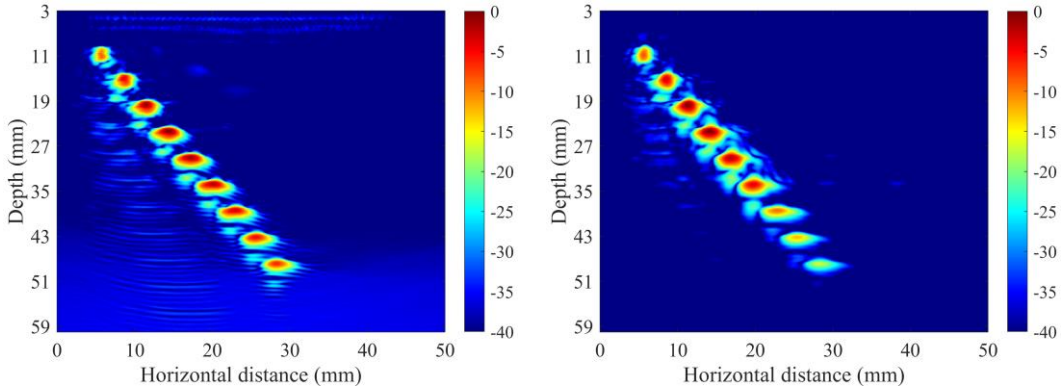

(**c**) ITFM (**d**) STSVD-ITFM

Figure 11. Imaging results of 2 mm diameter through-hole defects (no. 1 to no. 9).

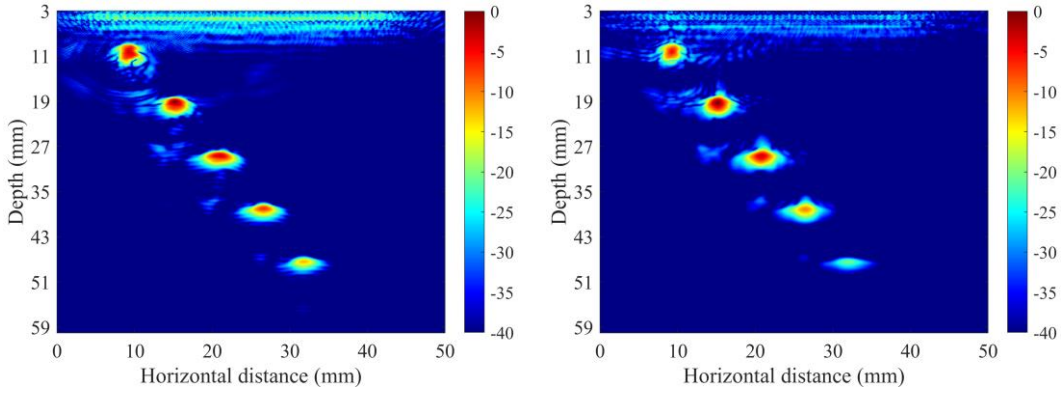

(**a**) TFM (**b**) STSVD-TFM

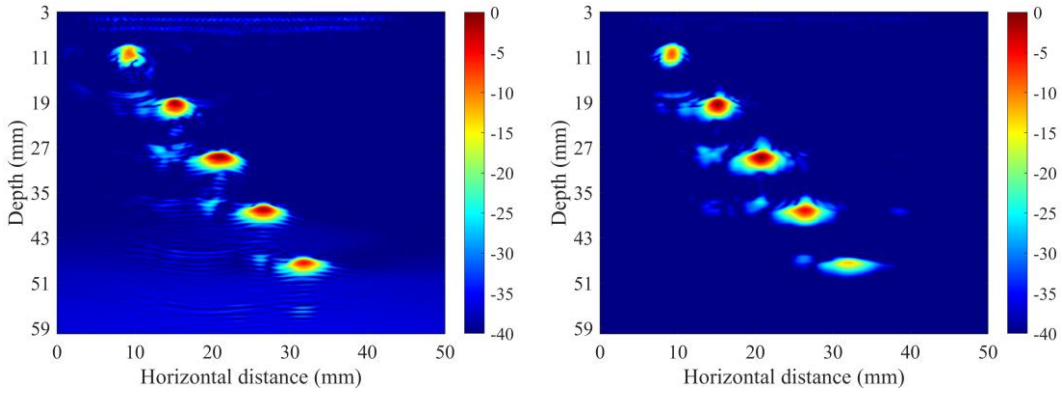

(**c**) ITFM (**d**) STSVD-ITFM

Figure 12. Imaging results of 3 mm diameter through-hole defects (no. 1 to no.5).

4.2. Analysis of Relevant Imaging Data

The pixel point amplitudes of three sizes of defects at a 50 mm depth location under different algorithms are extracted and depicted as curves for comparison, as shown in Figure 13. As expected, the ITFM algorithm processed images with the highest defective pixel point amplitudes. Due to the presence of a large number of artifacts in the image at this depth, the pixel point amplitude in the non-defective regions is higher than the rest of the image. The STSVD-ITFM algorithm reduces the pixel point amplitude in the non-defective regions of the ITFM image. The defective region amplitude is higher than the STSVD-TFM image and is similar to the TFM image. The overall level of pixel point

amplitude in the 1 mm defective region is higher than that of the TFM image. The STSVD-TFM algorithm reduces the pixel point amplitude of non-defective regions in the TFM image to a significantly lower level. This reduction also results in an overall lower pixel point amplitude of the defective region at that depth compared to the other three images.

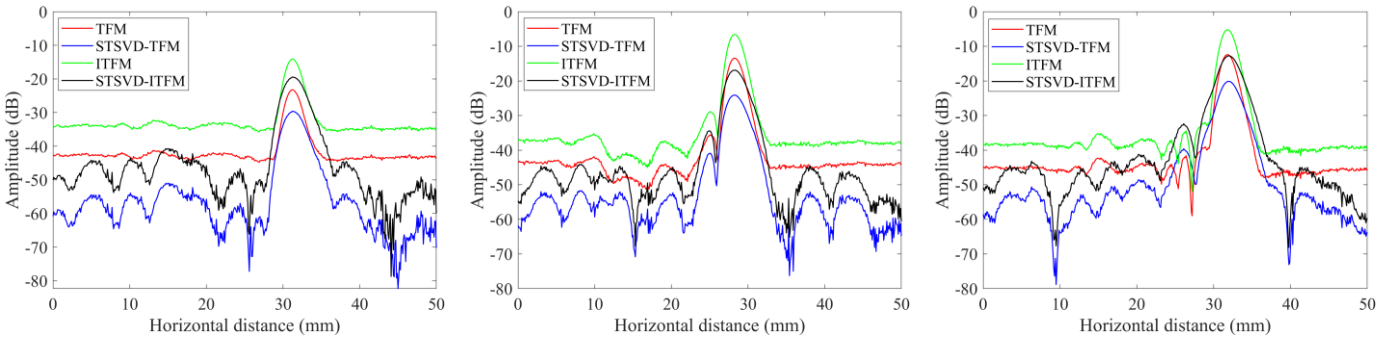

(**a**) 1 mm (**b**) 2 mm (**c**) 3 mm

Figure 13. Pixel point amplitude curves for each defect at 50 mm depth.

To quantitatively evaluate the imaging performance of each algorithm and to measure the image quality, comparisons are made by calculating the signal-to-noise ratio (SNR). The SNR is calculated as follows [34] :

$$SNR = 20\log_{10}\left|\frac{I_{\max}}{I_{\text{average}}}\right| \tag{13}$$

$$\text{SNR} = 20\log_{10}\left|\frac{I_{\max}}{I_{\text{average}}}\right|$$

where $I_{\max}$ is the maximum amplitude of the defective region and I_{average} is the average amplitude of the non-defective region. The higher the SNR value, the better the quality of the image.

The sum of the SNR for each defect in Figures 10–12 is calculated based on their pixel point amplitude. This sum is then divided by the total number of defects to find the average SNR. It is worth noting that the average amplitude of the non-defective region in the images is calculated by ignoring all the defect amplitudes and areas. The calculated average SNR results are shown in Figure 14 and Table 2.

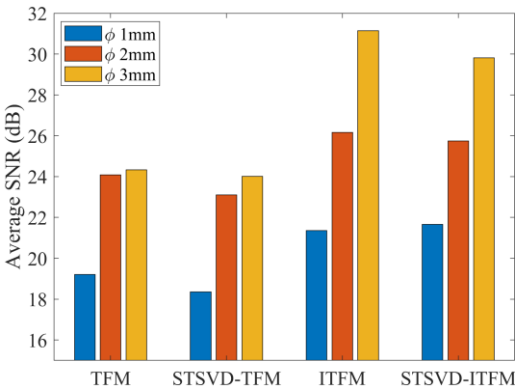

Figure 14. Comparison results of average SNR for three sizes of defects for each algorithm.

Table 2. Average SNR for three sizes of defects for each algorithm.

Type of Defect	Average SNR (dB)	
∅1 mm	19.20	TFM
	18.36	STSVD-TFM
	21.36	ITFM
	21.66	STSVD-ITFM
∅2 mm	24.09	TFM
	23.11	STSVD-TFM
	26.16	ITFM
	25.75	STSVD-ITFM
∅3 mm	24.33	TFM
	24.01	STSVD-TFM
	31.14	ITFM
	29.81	STSVD-ITFM

Both the ITFM and STSVD-ITFM algorithms show some improvement in average the SNR compared to the remaining two algorithms. The STSVD-ITFM algorithm has the highest average SNR in the imaging detection of 1 mm diameter through-hole defects. The STSVD-ITFM algorithm improves by 2.46 dB compared to the TFM algorithm, by 3.3 dB compared to the STSVD-TFM algorithm, and by 0.30 dB compared to the ITFM algorithm. The ITFM algorithm has the highest average SNR for the detection of 2 mm and 3 mm diameter cross-hole defects. The ITFM algorithm improved by 2.07 dB and 6.81 dB compared to the TFM algorithm, by 3.05 dB and 7.13 dB compared to the STSVD-TFM algorithm, and by 0.41 dB and 1.33 dB compared to the STSVD-ITFM algorithm, respectively. The average SNR of the STSVD-ITFM algorithm is improved by 1.66 dB and 5.48 dB compared to the TFM algorithm and by 1.64 dB and 5.80 dB compared to the STSVD-TFM algorithm, respectively.

The depth of the defect can be evaluated based on where the largest pixel point magnitude is located within its region. The results of depth quantification of different imaging algorithms for each size defect are shown in Table 3, Table 4, and Table 5, respectively.

Table 3. Depth quantitative results of 1 mm diameter through-hole defects (no. 1 to no. 9).

	Actual Depth (mm)	Measured Depth (mm)			
		TFM	STSVD-TFM	ITFM	STSVD-ITFM
no. 1	10.00	11.10	11.10	11.10	11.00
no. 2	15.00	15.40	15.40	15.40	15.40
no. 3	20.00	21.10	21.15	21.10	21.05
no. 4	25.00	25.10	25.10	25.10	25.00
no. 5	30.00	29.80	29.80	29.80	29.90
no. 6	35.00	34.60	34.50	34.60	34.60
no. 7	40.00	39.50	39.40	39.50	39.40
no. 8	45.00	44.10	44.00	44.10	44.20
no. 9	50.00	48.30	48.50	48.30	48.50
Average error (mm)		0.71	0.73	0.71	0.67

Table 4. Depth quantitative results of 2 mm diameter through-hole defects (no. 1 to no. 9).

	Actual Depth (mm)	Measured Depth (mm)			
		TFM	STSVD-TFM	ITFM	STSVD-ITFM
no. 1	10.00	10.60	10.90	10.60	10.40
no. 2	15.00	15.00	15.30	15.00	15.00
no. 3	20.00	19.70	19.70	19.70	19.80
no. 4	25.00	24.40	24.40	24.40	24.40
no. 5	30.00	29.20	29.20	29.20	29.40
no. 6	35.00	33.80	33.90	33.90	33.90
no. 7	40.00	38.50	38.50	38.50	38.40
no. 8	45.00	43.30	43.30	43.30	43.30
no. 9	50.00	48.00	48.00	48.00	48.10
Average error (mm)		0.96	1.02	0.96	0.92

Table 5. Depth quantitative results of 3 mm diameter through-hole defects (no. 1 to no. 5).

	Actual Depth (mm)	Measured Depth (mm)			
		TFM	STSVD-TFM	ITFM	STSVD-ITFM
no. 1	10.00	10.10	10.30	10.50	10.40
no. 2	20.00	19.20	19.30	19.20	19.50
no. 3	30.00	28.70	28.80	28.70	28.80
no. 4	40.00	38.10	38.20	38.10	38.20
no. 5	50.00	47.50	47.60	47.50	47.70
Average error (mm)		1.32	1.28	1.4	1.24

In the analysis of defect depth quantification, the imaging algorithms exhibit similar average error values, with the STSVD-ITFM algorithm demonstrating the smallest average errors. Specifically, the average error for 1 mm defects is approximately 0.7 mm, while for 2 mm and 3 mm defects, it is around 1.0 mm and 1.3 mm, respectively. It is observed that as the defect size increases, the quantitative error also increases, with the maximum error value remaining below 1.4 mm.

5. Conclusions

To ensure the weld quality of HDPE pipe butt-fusion joints, a STSVD-TFM imaging algorithm combined with ultrasonic phased array technology is proposed in this paper. FMC real-valued signal data are filtered using STSVD and used for improved ITFM algorithm imaging. Inspection of 1 mm, 2 mm, and 3 mm diameter through-hole defects in a HDPE material test block, distributed in depths of 10 mm to 50 mm, by extracting ultrasonic A-Scan signals of 1 mm diameter defects and comparing the imaging results of each algorithm, it is proved that STSVD is feasible to filter the FMC real-valued signal data directly. The ITFM algorithm can increase the amplitude of defects at deeper locations, but it introduces a lot of clutter and is less robust to background noise. The STSVD-ITFM algorithm has a better ability to suppress static clutter, which improves the disadvantage of the ITFM algorithm's poor robustness to background noise. The defect amplitude at deeper positions is higher than the STSVD-IFM algorithm. The STSVD-ITFM algorithm improves the average SNR by 3.30 dB, 1.66 dB, and 5.48 dB as compared to the TFM algorithm. In addition, the average errors of the STSVD-ITFM algorithm are smaller than the other three algorithms in all defect depth quantification results. The average errors are 0.67 mm, 0.92 mm, and 1.24 mm, respectively.

Author Contributions: Conceptualization, H.Z. and Q.W.; methodology, H.Z., Q.W., J.Z., L.W., W.X., and H.W.; software, H.Z. and Q.W.; validation, H.Z. and Q.W.; formal analysis, H.Z. and Q.W.; investigation, H.Z. and Q.W.; resources, Q.W.; data curation, H.Z. and Q.W.; writing—original draft preparation, H.Z. and Q.W.; writing—review and editing, H.Z., Q.W., J.Z., L.W., W.X., and H.W.; supervision, Q.W.; project administration, Q.W; funding acquisition, Q.W. All authors have read and agreed to the published version of the manuscript.

Funding: This research was supported by the National Key Research and Development Program of China (No. 2023YFF0611600) and the "Leading Talents Program" of Zhejiang Province Key Research and Development Program (No. 2022C03179).

Data Availability Statement: The original contributions presented in the study are included in the article, further inquiries can be directed to the corresponding author.

Conflicts of Interest: The authors declare no conflicts of interest.

References

1. Gong, Y.; Wang, S.-H.; Zhang, Z.-Y.; Yang, X.-L.; Yang, Z.-G.; Yang, H.-G. Degradation of Sunlight Exposure on the High-Density Polyethylene (HDPE) Pipes for Transportation of Natural Gases. *Polym. Degrad. Stab.* **2021**, *194*, 109752. https://doi.org/10.1016/j.polymdegradstab.2021.109752.
2. Guo, H.; Rinaldi, R.G.; Tayakout, S.; Broudin, M.; Lame, O. The Correlation between the Mixed-Mode Oligo-Cyclic Loading Induced Mechanical and Microstructure Changes in HDPE. *Polymer* **2021**, *224*, 123706. https://doi.org/10.1016/j.polymer.2021.123706.
3. Kim, J.-S.; Oh, Y.-J.; Choi, S.-W.; Jang, C. Investigation on the Thermal Butt Fusion Performance of the Buried High Density Polyethylene Piping in Nuclear Power Plant. *Nucl. Eng. Technol.* **2019**, *51*, 1142–1153. https://doi.org/10.1016/j.net.2019.02.002.
4. Pokharel, P.; Kim, Y.; Choi, S. Microstructure and Mechanical Properties of the Butt Joint in High Density Polyethylene Pipe. *Int. J. Polym. Sci.* **2016**, *2016*, 6483295. https://doi.org/10.1155/2016/6483295.
5. Lai, H.; Fan, D.; Liu, K. The Effect of Welding Defects on the Long-Term Performance of HDPE Pipes. *Polymers* **2022**, *14*, 3936. https://doi.org/10.3390/polym14193936.
6. Shi, J.; Feng, Y.; Tao, Y.; Guo, W.; Yao, R.; Zheng, J. Evaluation of the Seismic Performance of Butt-Fusion Joint in Large Diameter Polyethylene Pipelines by Full-Scale Shaking Table Test. *Nucl. Eng. Technol.* **2023**, *55*, 3342–3351. https://doi.org/10.1016/j.net.2023.06.013.
7. Egerton, J.S.; Lowe, M.J.S.; Huthwaite, P.; Halai, H.V. Ultrasonic Attenuation and Phase Velocity of High-Density Polyethylene Pipe Material. *J. Acoust. Soc. Am.* **2017**, *141*, 1535–1545. https://doi.org/10.1121/1.4976689.
8. Lai, H.S.; Tun, N.N.; Yoon, K.B.; Kil, S.H. Effects of Defects on Failure of Butt Fusion Welded Polyethylene Pipe. *Int. J. Press. Vessel. Pip.* **2016**, *139–140*, 117–122. https://doi.org/10.1016/j.ijpvp.2016.03.010.
9. Djebli, A.; Bendouba, M.; Aid, A.; Talha, A.; Benseddiq, N.; Benguediab, M. Experimental Analysis and Damage Modeling of High-Density Polyethylene under Fatigue Loading. *Acta Mech. Solida Sin.* **2016**, *29*, 133–144. https://doi.org/10.1016/S0894-9166(16)30102-1.
10. Majid, F.; Elghorba, M. HDPE Pipes Failure Analysis and Damage Modeling. *Eng. Fail. Anal.* **2017**, *71*, 157–165. https://doi.org/10.1016/j.engfailanal.2016.10.002.
11. Ur Rahman, M.S.; Haryono, A.; Abou-Khousa, M.A. Microwave Non-Destructive Evaluation of Glass Reinforced Epoxy and High Density Polyethylene Pipes. *J. Nondestruct. Eval.* **2020**, *39*, 26. https://doi.org/10.1007/s10921-020-00669-2.
12. Zheng, J.; Zhang, Y.; Hou, D.; Qin, Y.; Guo, W.; Zhang, C.; Shi, J. A Review of Nondestructive Examination Technology for Polyethylene Pipe in Nuclear Power Plant. *Front. Mech. Eng.* **2018**, *13*, 535–545. https://doi.org/10.1007/s11465-018-0515-9.
13. Frederick, C.; Porter, A.; Zimmerman, D. High-Density Polyethylene Piping Butt-Fusion Joint Examination Using Ultrasonic Phased Array. *J. Press. Vessel. Technol.* **2010**, *132*, 051501. https://doi.org/10.1115/1.4001212.
14. Lacaze, B. Random Propagation Times for Ultrasonics through Polyethyilene. *Ultrasonics* **2021**, *111*, 106313. https://doi.org/10.1016/j.ultras.2020.106313.
15. Zheng, J.; Hou, D.; Guo, W.; Miao, X.; Zhou, Y.; Shi, J. Ultrasonic Inspection of Electrofusion Joints of Large Polyethylene Pipes in Nuclear Power Plants. *J. Press. Vessel. Technol.* **2016**, *138*, 060908. https://doi.org/10.1115/1.4033448.
16. Qin, Y.; Shi, J.; Zheng, J.; Hou, D.; Guo, W. An Improved Phased Array Ultrasonic Testing Technique for Thick-Wall Polyethylene Pipe Used in Nuclear Power Plant. *J. Press. Vessel. Technol.* **2019**, *141*, 041403. https://doi.org/10.1115/1.4043384.
17. Behravan, A.; Tran, T.Q.; Li, Y.; Davis, M.; Shaikh, M.S.; DeJong, M.M.; Hernandez, A.; Brand, A.S. Field Inspection of High-Density Polyethylene (HDPE) Storage Tanks Using Infrared Thermography and Ultrasonic Methods. *Appl. Sci.* **2023**, *13*, 1396. https://doi.org/10.3390/app13031396.
18. Holmes, C.; Drinkwater, B.W.; Wilcox, P.D. Post-Processing of the Full Matrix of Ultrasonic Transmit–Receive Array Data for Non-Destructive Evaluation. *NDT E Int.* **2005**, *38*, 701–711. https://doi.org/10.1016/j.ndteint.2005.04.002.
19. Lopez Villaverde, E.; Robert, S.; Prada, C. Ultrasonic Imaging in Highly Attenuating Materials With Hadamard Codes and the Decomposition of the Time Reversal Operator. *IEEE Trans. Ultrason. Ferroelectr. Freq. Control.* **2017**, *64*, 1336–1344. https://doi.org/10.1109/TUFFC.2017.2690499.

20. Zong, S.; Wang, S.; Luo, Z.; Wu, X.; Zhang, H.; Ni, Z. Robust Damage Detection and Localization Under Complex Environmental Conditions Using Singular Value Decomposition-Based Feature Extraction and One-Dimensional Convolutional Neural Network. *Chin. J. Mech. Eng.* **2023**, *36*, 61. https://doi.org/10.1186/s10033-023-00889-3.
21. Liu, C.; Harley, J.B.; Bergés, M.; Greve, D.W.; Oppenheim, I.J. Robust Ultrasonic Damage Detection under Complex Environmental Conditions Using Singular Value Decomposition. *Ultrasonics* **2015**, *58*, 75–86. https://doi.org/10.1016/j.ultras.2014.12.005.
22. Xu, L.; Chatterton, S.; Pennacchi, P. Rolling Element Bearing Diagnosis Based on Singular Value Decomposition and Composite Squared Envelope Spectrum. *Mech. Syst. Signal. Pract.* **2021**, *148*, 107174. https://doi.org/10.1016/j.ymssp.2020.107174.
23. Shahjahan, S.; Rupin, F.; Aubry, A.; Derode, A. Evaluation of a Multiple Scattering Filter to Enhance Defect Detection in Heterogeneous Media. *J. Acoust. Soc. Am.* **2017**, *141*, 624–640. https://doi.org/10.1121/1.4973954.
24. Cunningham, L.J.; Mulholland, A.J.; Tant, K.M.M.; Gachagan, A.; Harvey, G.; Bird, C. The Detection of Flaws in Austenitic Welds Using the Decomposition of the Time-Reversal Operator. *Proc. R. Soc. A—Math. Phys. Eng. Sci*. **2016**, *472*, 20150500. https://doi.org/10.1098/rspa.2015.0500.
25. Zhang, Y.; Gao, X.; Zhang, J.; Jiao, J. An Ultrasonic Reverse Time Migration Imaging Method Based on Higher-Order Singular Value Decomposition. *Sensors* **2022**, *22*, 2534. https://doi.org/10.3390/s22072534.
26. Rao, J.; Zeng, L.; Liu, M.; Fu, H. Ultrasonic Defect Detection of High-Density Polyethylene Pipe Materials Using FIR Filtering and Block-Wise Singular Value Decomposition. *Ultrasonics* **2023**, *134*, 107088. https://doi.org/10.1016/j.ultras.2023.107088.
27. Demene, C.; Deffieux, T.; Pernot, M.; Osmanski, B.-F.; Biran, V.; Gennisson, J.-L.; Sieu, L.-A.; Bergel, A.; Franqui, S.; Correas, J.-M.; et al. Spatiotemporal Clutter Filtering of Ultrafast Ultrasound Data Highly Increases Doppler and fUltrasound Sensitivity. *IEEE Trans. Med. Imaging* **2015**, *34*, 2271–2285. https://doi.org/10.1109/TMI.2015.2428634.
28. Al Mukaddim, R.; Weichmann, A.M.; Mitchell, C.C.; Varghese, T. Enhancement of In Vivo Cardiac Photoacoustic Signal Specificity Using Spatiotemporal Singular Value Decomposition. *J. Biomed. Opt*. **2021**, *26*, 046001. https://doi.org/10.1117/1.JBO.26.4.046001.
29. Baranger, J.; Arnal, B.; Perren, F.; Baud, O.; Tanter, M.; Demene, C. Adaptive Spatiotemporal SVD Clutter Filtering for Ultrafast Doppler Imaging Using Similarity of Spatial Singular Vectors. *IEEE Trans. Med. Imaging* **2018**, *37*, 1574–1586. https://doi.org/10.1109/TMI.2018.2789499.
30. Rao, J.; Qiu, H.; Teng, G.; Al Mukaddim, R.; Xue, J.; He, J. Ultrasonic Array Imaging of Highly Attenuative Materials with Spatio-Temporal Singular Value Decomposition. *Ultrasonics* **2022**, *124*, 106764. https://doi.org/10.1016/j.ultras.2022.106764.
31. Zhang, H.; Bai, B.; Zheng, J.; Zhou, Y. Optimal Design of Sparse Array for Ultrasonic Total Focusing Method by Binary Particle Swarm Optimization. *IEEE Access* **2020**, *8*, 111945–111953. https://doi.org/10.1109/ACCESS.2020.3001947.
32. Zhu, W.; Xiang, Y.; Zhang, H.; Cheng, Y.; Fan, G.; Zhang, H. Research on Ultrasonic Sparse DC-TFM Imaging Method of Rail Defects. *Measurement* **2022**, *200*, 111690. https://doi.org/10.1016/j.measurement.2022.111690.
33. Hu, H.; Du, J.; Xu, N.; Jeong, H.; Wang, X. Ultrasonic Sparse-TFM Imaging for a Two-Layer Medium Using Genetic Algorithm Optimization and Effective Aperture Correction. *NDT E Int.* **2017**, *90*, 24–32. https://doi.org/10.1016/j.ndteint.2017.05.002.
34. Teng, D.; Liu, L.; Xiang, Y.; Xuan, F.-Z. An Optimized Total Focusing Method Based on Delay-Multiply-and-Sum for Nondestructive Testing. *Ultrasonics* **2023**, *128*, 106881. https://doi.org/10.1016/j.ultras.2022.106881.